HYBRID TURBULENCE MODELS EVALUATION FOR ROTORCRAFT FLOWS

Florent Dehaeze and George N. Barakos

CFD Laboratory, Department of Engineering
University of Liverpool, L69 3GH, U.K.
http://www.liv.ac.uk/flightscience/PROJECTS/CFD/ROTORCRAFT/RBD/index.htm
Email: Florent.Dehaeze@liv.ac.uk, G.Barakos@liverpool.ac.uk

Abstract

The CFD prediction of rotor loads and vibration is influenced by the resolved part of the flow spectrum. Mainstream CFD methods, currently in routine use for rotors, employ the URANS approach that is inherently limited in terms of the size and frequency of the resolved structures. This paper attempts to take things further by applying hybrid methods of turbulence modelling and simulation aiming to resolve a larger part of the spectrum around blades in hover and forward flight. At first, results for several DES closures are presented for the flow around a stalled aerofoil. The calculations reveal some of the advantage of DES over URANS as well as some of the performance issues associated with DES. A comparison between DES and RANS follows for the case of a forward flying rotor suggesting that DES is capable of resolving higher harmonics in the loads. The limitations of the available experiments are also highlighted.

NOMENCLATURE

c Chord length

C_{b1} Production correction factor in the SALSA model

$c_{b1}, c_{b2}, c_{w1}, c_{w3}, c_{t3}, c_{t4}$ SA turbulence model constants

C_{DES} Mesh length scale scaling in the DES and DDES models

$\tilde{d}$ DES and DDES models length scale

d Wall-distance

DES Delayed Detached-Eddy Simulation

DDES SALSA Delayed Detached-Eddy Simulation with the SALSA production term modification

DES Detached-Eddy Simulation

DES SALSA Detached-Eddy Simulation with the SALSA production term modification

d_t Distance from the field point to the trip

f_d B function in the DDES model

$f_{t1}, f_{t2}, f_{v2}, f_{v1}, f_w$ SA turbulence model empirical functions

l_{RANS} RANS model length scale

M Mach number

M_∞ Freestream Mach number

M^2C_M Mach scaled moment coefficent

M^2C_N Mach scaled normal coefficent

$P_{\tilde{\nu_t}}$ Production term in the SALSA model

R Rotor radius

RANS Reynolds Averaged Navier-Stokes

r_d Root of the ratio between the length scale and the wall distance

Re Reynolds number

S Vorticity magnitude

SALSA Strain Adaptative Linear Spalart-Allmaras model

SA Spalart-Allmaras model

St Strouhal number

U_∞ Freestream velocity

URANS Unsteady Reynolds Average Navier-Stokes

C_T Rotor thrust coefficient

α_S Shaft angle of the rotor, positive backward

β_0 Coning angle of the rotor

β_{1c},β_{1s} Cyclical flapping angle of the rotor

χ Ratio of the undamped viscosity and the molecular viscosity $\chi = \tilde{\nu}/\nu$

ΔU Difference between the velocity at the field point

Δx Grid spacing along the wall at the trip

Δ Mesh length scale

δ Boundary layer thickness

$\Delta_x, \Delta_y, \Delta_z$ Mesh length scale

κ Kármán constant

μ Forward flight advance ratio

ν Molecular viscosity

ν_t Kinematic eddy viscosity

ω_t	Wall vorticity at the trip
σ	Turbulent Prandtl number
θ_0	Collective angle of the rotor
θ_{1c},θ_{1s}	Cyclical pitch angle of the rotor
$\tilde{\nu}$	Undamped eddy viscosity

1 INTRODUCTION

Rotorcraft calculations are still challenging due to the unsteady flow nature, the coupled aerodynamics and aeroelasticity of blades and the presence of wakes in the vicinity of the rotor characterised by a range of flow scales, both laminar and turbulent. Currently, URANS models are widely used in the rotorcraft domain. However, due to their limitations, these models could be unadapted to the specificities of rotorcraft flows: in particular, the cutoff frequency of URANS is at about 1000Hz, which could be too low to predict all the phenomena occurring in rotorcraft flow, with blades usually rotating at 300RPM and within a vortical wake. An alternative could be hybrid RANS/LES models in the form of Detached-Eddy Simulation [11] (DES) or Limited Numerical Scales [1] (LNS) . Furthermore, hybrid models can be used to increase the fidelity of CFD predictions at the edges of the flying domain where stalled flow is encountered.

For the above reasons, the present study attempts to assess DES closures for flows pertinent to rotorcraft and provide insight in the suitability of DES for rotor flows. After presenting the models, two cases are considered, including stalled flow around a NACA0021 aerofoil and the ONERA 7AD in forward flight.

2 TURBULENCE MODELS AND CFD METHODS

2.1 Spalart-Allmaras Model

The one-equation Spalart-Allmaras (SA) turbulence model [12] solves a transport equation for the eddy viscosity directly. The kinematic eddy viscosity, (ν_t), in the SA model is calculated by

$$\nu_t = \tilde{\nu} \cdot f_{v1} \quad , \tag{1}$$

where

$$f_{v1} = \frac{\chi^3}{\chi^3 + c_{v1}^3} \quad \text{and} \quad .\chi = \frac{\tilde{\nu}}{\nu}$$

In the above equations, and hereafter, the term f refers to a function, c refers to a constant, ν is the molecular viscosity and $\tilde{\nu}$ is the undamped eddy viscosity that obeys the following transport equation:

$$\frac{D\tilde{\nu}}{Dt} = c_{b1}\left(1 - f_{t2}\right)\tilde{S}\tilde{\nu} \tag{2}$$

$$+ \frac{1}{\sigma}\left(\bigtriangledown \cdot \left(\left(\nu + \tilde{\nu}\right) \bigtriangledown \tilde{\nu}\right) + c_{b2}\left(\bigtriangledown\tilde{\nu}\right)^2\right) \tag{3}$$

$$- \left(c_{w1} f_w - \frac{c_{b1}}{\kappa^2} f_{t2}\right)\left(\frac{\tilde{\nu}}{d}\right)^2 + f_{t1}\Delta U^2 \quad . \tag{4}$$

The first term on the right-hand side is the production term, the second is the diffusion term and the third is the near-wall term. The last term models transition downstream of tripping. The subscript b stands for *basic*, w for *wall* and t for *trip*. The parameter σ represents the turbulent Prandtl number and d is the wall-distance.

The term $\tilde{S}$ in Equation (2) is defined by the following equation, where S is the vorticity magnitude:

$$\tilde{S} = S + \frac{\tilde{\nu}}{k^2 d^2} f_{v2} \quad , \tag{5}$$

$$f_{v2} = 1 - \frac{\chi}{1 + \chi f_{v1}} \quad . \tag{6}$$

The function f_w in Equation (2) is given by:

$$\begin{aligned} f_w &= g\left(\frac{1 + c_{w3}^6}{g^6 + c_{w3}^6}\right)^{1/6} \quad , \\ g &= r + c_{w2}\left(r^6 - r\right) \quad , \\ r &= \frac{\tilde{\nu}}{\tilde{S} k^2 d^2} \end{aligned} \tag{7}$$

The f_{t2} function is defined by:

$$f_{t2} = c_{t3} \cdot e^{-c_{t4} \cdot \chi^2} \quad . \tag{8}$$

The trip function f_{t1} is defined as

$$f_{t1} = c_{t1} g_t \cdot e^{-c_{t2} \frac{\omega_t^2}{\Delta U^2}\left(d^2 + g_t^2 d_t^2\right)} \quad , \tag{9}$$

where d_t is the distance from the field point to the trip, ω_t is the wall vorticity at the trip, ΔU is the difference between the velocity at the field point and that at the trip and $g_t = \min\left(0.1, \Delta U / \omega_t \Delta x\right)$, in which Δx is the grid spacing along the wall at the trip.

Values used for the S-A turbulence model constants are given in Table 1. The constant c_{w1} is defined as

$$c_{w1} = \frac{c_{b1}}{k^2} + \frac{\left(1 + c_{b2}\right)}{\sigma} = 3.2391 \quad . \tag{10}$$

A value of 2/3 has been used for the turbulent Prandtl number, σ.

2.2 The SALSA Modified Spalart-Allmaras Model

The SA model tends to over-predict the turbulent eddy viscosity in vortex cores. Therefore, a limiter was introduced by Rung in [9] to counter this problem. The production term was consequently modified in order to limit the turbulence production. The new production term is defined as a product of a shear stress function, the undamped viscosity and a factor C_{b1}:

$$P_{\tilde{\nu}_t} = \tilde{\nu}_t \tilde{S} C_{b1} \quad . \tag{11}$$

This factor C_{b1} is defined as:

$$C_{b1} = 0.1355\sqrt{\Gamma} \quad , \tag{12}$$

with

$$\begin{aligned} \Gamma &= \min\left[1.25, max\left(\gamma, 0.75\right)\right] \quad , \\ \gamma &= \max\left(\alpha_1, \alpha_2\right) \quad , \\ \alpha 1 &= \left[1.01\left(\tilde{\nu}_t / \kappa^2 d^2 S^*\right)\right]^{0.65} \quad , \\ \alpha 2 &= \max\left[0, 1 - tanh\left(\chi/68\right)\right]^{0.65} \quad , \end{aligned}$$

where $S^* = \sqrt{2\tilde{S^*}_{ij}\tilde{S^*}_{ij}}$ with $\tilde{S^*}_{ij}$ representing the shear-stress tensor.

The α_1 term allows the damping of the excessive production in high strains, while the α_2 term avoids unwanted wall damping.

2.3 Detached-Eddy Simulation (DES)

Despite its potential, the need of fine grids close to the wall does not allow the use of LES in complex flows. Detached-Eddy Simulation may be an alternate. The main principle of these models is the use of RANS close to the walls and LES further.

The original idea of DES was postulated by Spalart *et al.* [11]. The RANS equations with a modified length scale are used in the whole domain, though the length scale is also depending on the mesh size. In the RANS areas, the usual RANS length scale will be used, but in the LES zones, the length scale will now depend on the mesh length scale, forcing the turbulence model to behave like LES. DES does not need an interface between the RANS and LES part.

Spalart introduced the mesh length scale Δ as a function of the cell size following the three axis Δ_x, Δ_y and Δ_z:

$$\Delta = max(\Delta_x, \Delta_y, \Delta_z) \quad . \tag{13}$$

The new length scale for DES is then:

$$l_{DES} = min(l_{RANS}, C_{DES}\Delta) \quad , \tag{14}$$

where C_{DES} is an arbitrary constant. For example, in the case of the SA model, the scale length l_{RANS} is the wall distance d. In the new DES model, the length scale $\tilde{d}$ is defined as:

$$\tilde{d} = \min\left(d, C_{DES}\Delta\right) \quad . \tag{15}$$

Therefore, near walls, the model will use the RANS equations, and further away, the length scale will switch to the grid length scale and the model will behave like LES.

This modification aims at increasing the dissipation term of the turbulent kinetic energy and thus decrease the production term. The dissipation term is now equal to:

$$-C_{w1}f_{w1}\left(\frac{\tilde{\nu}}{\tilde{d}}\right)^2 \quad . \tag{16}$$

2.4 Delayed Detached-Eddy Simulation (DDES)

DES may also have problems with the transition between the LES and RANS zones. For coarse meshes around the wall, DES will work as expected with a transition to LES outside the boundary layer. However, if the mesh is fine ($\Delta = \delta/20$, with δ the boundary layer thickness), then the simulation will behave like a Wall-Modelled LES (LES with RANS as a wall model). Problems appear for mesh sizes between these two cases, where the transition to LES takes place at about the first third of the boundary layer. Two thirds of the boundary layer will then be in LES mode. This will reduce turbulent viscosity and therefore the Reynolds stresses.

To counter this, Spalart [10] developed the Delayed Detached-Eddy Simulation (DDES). DDES introduces a limiter in the length scale to ensure that transition will not take place inside the boundary layer. In the Spalart-Allmaras model, this limiter modifies the parameter r (root of the ratio between the length scale and the wall distance):

$$r_d = \frac{\nu_t + \nu}{\sqrt{\frac{\partial U_i}{\partial x_j}\frac{\partial U_i}{\partial x_j}\kappa^2 d^2}} \quad , \tag{17}$$

with κ the Kármán constant. The term $\nu_t + \nu$ can be replaced with $\tilde{\nu}$ in the SA model. Now r_d equals 1 in the logarithmic part of the boundary layer and equals 0 outside the boundary layer. ν avoids this zero r_d values close to the wall. A new function f_d is defined as:

$$f_d = 1 - \tanh\left(\left[Ar_d\right]^B\right) \quad . \tag{18}$$

f_d equals 1 in the LES zones and 0 elsewhere. The A and B values are arbitrary and set the shape of f_d. The values chosen to obtain good results for a plane wall flow are $A = 8$ and $B = 3$.

The new value of the length scale un the Spalart-Allmaras model is now set at:

$$\tilde{d} = d - f_d \max\left(0, d - C_{DES}\Delta\right) \quad . \tag{19}$$

The RANS zone is defined by $f_d = 0$ and the LES zone by $f_d = 1$. In the case of highly detached flows, the detached zone is calculated in LES mode and the transition is quicker, allowing a smaller grey zone.

2.5 CFD Method

The HMB code of Liverpool was used for solving the flow around the blades. HMB is a Navier-Stokes solver employing multi-block structured grids. For rotor flows, a typical multi-block topology used in the University of Liverpool is described in [7]. The multi-block topology allows for an easy sharing of the calculation load for parallel computing. A C-mesh is used around the blade and this is included in a larger H structure which fills up the rest of the computational domain. The block boundaries on a forward flying ONERA 7A rotor is shown in black in Figure 11b. Rotor trimming, corresponding to rigid movements of the blade, is obtained by a rigid motion of the whole C-Part of the mesh, shown in grey in Figure 11b. This preserves the mesh quality around the blade surface. The layer of blocks around the C-part is then re-meshed using Trans-Finite Interpolation method [2].

The code solves the governing equations using a cell-centred finite volume method. The convective terms are discretised using either Osher's [6] or Roe's [8] scheme. MUSCL interpolation is used to provide formally third order accuracy and the Van Albada limiter is used to avoid spurious oscillations across shocks. The time-marching of the solution is based on the implicit, dual time-stepping method of Jameson [4]. The final algebraic system of equations is solved using the Generalised Conjugate Residual method, in conjunction with Block Incomplete Lower-Upper factorisation. A number of turbulence models including one and two-equation statistical models as well as LES and DES formulations have been implemented into the code . More details of the employed CFD solver and turbulence models are given in Nayyar *et al.* [5].

3 STALLED FLOW AROUND A NACA0021 AEROFOIL

A first assessment concerned the experiment of Swalwell and Sheridan [13]. The NACA0021 is a thick airfoil and at a high incidence of 60^o behaves like a bluff body with a Kármán way in its wake. This test case involving a lifting body with a highly detached flow was found to be interesting for assessing the performance of the DES models.

3.1 Test Case Description

The NACA0021 aerofoil shown in Figure 1 was tested in the post stall regime by Swalwell in [13]. The experiment covered incidences from 20 to 90 degrees at Reynolds number of 2.7×10^5 and Mach number of 0.10. The wing had a length of 7.2 chords and was in contact with both sides of the wind tunnel in order to approximate infinite wing conditions. Pressure measurements were conducted on two airfoils sections at one chord even, around the wing mid-span.

The European research program DESider used this experiment as a test case to assess DES models. Lift and drag coefficients of 0.931 and 1.517 were obtained from pressure measurements at this particular incidence. Measurements of frequency content of these coefficients were also carried out. Two peaks appear in their Fourier transform at Strouhal numbers of about 0.200 and about 0.400, equivalent to frequencies of 54.45Hz and 108.90Hz respectively. The Strouhal number is the frequency non-dimensionalised with the references length and speed. In this particular case, the freestream velocity and the chord length are used:

$$St = f\frac{c}{U_\infty}\,. \tag{20}$$

The flow was computed on a grid with about 1.1 million nodes on a mesh covering 2 chord length of span. An O-topology was used. Symmetry boundary conditions are used on both planes at the tips of the wing. The farfield is located at 15 chords. The trailing edge was sharpened for the calculation. The tested turbulence models are the standard Spalart-Allmaras (S-A), the Detached-Eddy Simulation (DES) and the Delayed Detached-Eddy Simulation (DDES). These models were also tested with the SALSA production term modification. Finally, an assessment of the effect of the filtering C_{DES} coefficient was carried out by repeating the same calculation with a halved C_{DES} coefficient. The grid supplied by the NTS[1] was also tested as well as a double sized version of the coarse grid.

A $2c$ span size was chosen following the length advised by Guenot [3]. Guenot's study was performed for an incidence of 45 degrees and DESider members found this length the be underestimated, probably because of the change in incidence. A length of $2.8c$ would be more adapted.

3.2 Flow Properties

The hybrid turbulence models resulted in an unsteady fully 3D flow with a Kármán way in the wake. Long streamwise structures are also visible through Q-criterion isosurfaces shown in Figure 9. An alternation of low and high shedding activity is recognised with smaller and stronger variations of the lift coefficient as well as lower and higher pressure in the vortices cores. This shedding activity variation is not predicted similarly by all turbulence models though.

A mean pressure coefficient repartition on the airfoil section is shown in Figure 2. The prediction is quite good but the suction on the upper surface is slightly underpredicted for the calculations that gave a steady flow and overpredicted for the other ones. The experimental error margin was however not given and the experimental measurements are located inside the computed RMS bars of the computed pressure coefficient for calculations with an unsteady result.

The mean flow shown in Figure 10 is dominated by the main leading and trailing edge vortices, with the leading edge vortex being bigger than the trailing one. The junction between both is located between 65 and 75% of the chord. The mean flow topology is the same for all models, whether they end up with a steady or unsteady flow.

The upper surface pressure was more thoroughly studied at four locations on the aerofoil upper surface. These locations are equally spaced on the upper surface as shown in Figure 1. The pressure spectral density at these locations is shown in Figure 6. The spectrum is dominated by the main shedding frequency and probes 26, 35 and 50 correspond to a flow dominated by the influence of one vortex only. However the spectrum at the probe 41 has two peaks, one at the main shedding frequency and one at twice this frequency. This shows that at this location, the influence of both vortices alternates.

The correlation at -1 (with a small lag) between the leading and trailing edges shows phase opposition in the creation of the leading and trailing edge vortices. The correlation between probes 26 and 35 shows that the flow at both locations is dominated by the same vortex, with a slight lag due to the position offset. The lower correlation between probes 35 and 41 seems to come from the fact that the limit between the trailing and leading edge vortices is located in between these probes and at least probe 41 is located on the area where the leading edge and trailing edge vortices are dominant alternatively.

3.3 Comparison of the Various Turbulence Models with the Experiment

The first main difference between the calculations comes from the flow properties: while the URANS models converged to a steady flow, the hybrids one converged to a fully unsteady flow. A part of the lift coefficient evolution during the unsteady calculations is shown in Figure 7. While the DES with a halved C_{DES} coefficient seems to accurately predict the evolution of the shedding activity with lows and highs which are visible as lowering or increases of the lift coefficient evolution, the DES and DDES-SALSA seemed to underpredict it and the DDES did not predict any shedding activity.

The mean lift and drag coefficients are presented in Table 2. The hybrid turbulence models overestimate the drag, and underestimate the lift. The URANS models on the other

[1] New Technologies and Services

hand predicted an accurate drag coefficient but the lift coefficient is largely underestimated. The power spectra density of the lift and drag coefficients obtained with the various calculations with fully unsteady flow are compared in Figure 3. The two first peaks of both coefficients are well predicted by the calculations that were fully unsteady but tend to have a slightly higher amplitude than the experiment. Most of the models also predict other peaks at higher frequencies while these peaks are not present in the experiment. Only the DES with half C_{DES} does not predict these. Furthermore the slope on the drag coefficient FFT at higher frequencies is overpredicted, particularly in the case of the DDES SALSA, which also predicted the highest peaks at higher frequencies. The slope is too steep in the full spectrum of the drag coefficient FFT and depends on the turbulence model. The use of a lowered C_{DES} seems to bring better results.

A comparison of the mean pressure coefficient, shown in Figure 2, reveals that the URANS models underpredicted the suction on the upper surface, and the hybrid turbulence models appear to slightly overpredict of this suction. The DES with a halved C_{DES} coefficient and the DES SALSA seem to give slightly better predictions while the difference between the DES and DDES is small probably due to the coarseness of the grid. The transition between the RANS and LES part was probably taking part outside of the boundary layer already, meaning that the shaping function in the DDES formulation did not have any influence. The DDES SALSA leads to an overprediction.

Flow visualisation in the mid-plane of the wing obtained with models leading to a steady flow is shown in Figure 8. Instantaneous contours of Mach number obtained by the unsteady calculations as well as pressure distribution in slices perpendicular to the wing are shown in Figure 9. The calculations that predicted the strongest variations in shedding activities tend to also predict bigger structures in the streamwise direction. The comparison of the mean flow for the various calculations in Figure 10 shows that, while the mean flow structure is the same for every calculation, the leading edge vortex tends to be bigger in size and its centre further back when the calculation goes steady.

4 DES APPLIED ON A ROTOR

Encouraged by the DES results for the stalled aerofoil case, rotors in forward flight were then attempted. Due to its popularity in CFD works and the availability of experimental data from several wind tunnel campaigns, the ONERA 7A/7AD rotors, described in Figure 11a, were considered. The CFD mesh for the forward flying rotor is shown in Figure 11b and consists of a C-type within an H-type topology. The grid was generated for a single blade and for the collective and coning settings shown in Table 3. For this complex topology there was less flexibility to optimise the mesh for DES though care has been taken to refine the mesh near the blades while maintaining some of the mesh orthogonality at the rotor disk plane where the wake is expected to be concentrated. The mesh for the complete rotor was put together by copying the single-blade mesh and rotating it around the azimuth.

The computation was undertaken using 16.8 million nodes with good load balancing and due to CPU time limitations only three rotor revolutions were attempted using an azimuthal step of 0.25 degrees. This time step appears to be close to what is used for URANS computations though further refinement would lead to overwhelmingly expensive computations.

The results obtained from the URANS and the DES solutions are compared against experimental data in Figure 12 for case 3 of Table 3. Three stations are shown corresponding to 0.7, 0.825 and 0.9 of the rotor radius. Inboards, the flow appears to be well-resolved by both the DES and the URANS solutions and the overall agreement for the Mach-scaled normal force coefficient is good on the advancing side of the blade and the rear of the disk. Some difference exist on the retreating side and the DES solution fares somehow better in that region. This is especially true for the pitching moment coefficient. At the $r/R = 0.825$ station, the situation shows some of the DES benefits though these are mainly concentrated on the retreating side. For the selected test case, the experimental data show the presence of some blade-vortex-interaction near 100 degrees of azimuth. None of the employed models captured the BVI and this is apparently due to the lack of spanwise mesh resolution as well as the selected azimuthal step of 0.25 degrees. Interestingly, the depth of the normal force coefficient on the advancing side of the rotor is well-captured in terms of magnitude and phase by both models. For the third available station ($r/R = 0.975$) the URANS and DES results are fairly close for the pitching moment and normal force coefficients. Again, it is interesting to see that regardless of some minor differences near the advancing side, both models follow the trend of the experiments quite accurately. The only exception is the for the BVI encountered at azimuth angles of about 100 degrees that does not appear to be resolved.

Further insight in the differences and similarities of the models can be obtained by looking at the Q-criterion iso-surfaces for a case 2 simulation in Figure 13. The overall distribution and shape of the surfaces looks similar between URANS and DES. The DES solution, however, appears to have more fine structures super-imposed on some mean flow field. This prompted further investigation in the data and for this reason, the mean blade loads as well as the first harmonic were removed from the rotor-integrated forcing. The results are shown in Figure 14 and it appears that at the front of the disk as well as the advancing side, the two solutions are very close to each other. For the back of the disk, the situation is different. The DES solution, shows higher peak-to-peak variations and higher level of oscillations that diminish as the inflow of the rotor disk is approaching. This suggests that since no forcing has been used for the computations near the free-stream, the DES behaved more-or-less like URANS for that part of the flow domain. The presence of the vortices and the complex wake further downstream has triggered the LES part of the DES model and much reduced levels of eddy-viscosity were observed. For this reason, more and more flow structures were resolved on the relatively coarse DES mesh.

From the available experiment, it is difficult to extract information about the level of turbulence present around the rotor. The use of DES is therefore only suitable for qualitative comparisons. On the other hand, based on the simpler cases studied for flows around aerofoils, DES appears to have

Coefficient	c_{b1}	σ	c_{b2}	κ	c_{w2}	c_{w3}	c_{v1}	c_{t1}	c_{t2}	c_{t3}	c_{t4}
Value	0.1355	2/3	0.622	0.41	0.3	2	7.1	1	2	1.1	2

Table 1: Closure coefficients for the SA model

some merit. Clearly, experiments providing detailed spectra are needed to screen DES models and help improve the predictions of CFD.

5 CONCLUSIONS

The efficiency of some DES models against URANS models has been assessed on a stalled aerofoil. The results showed some improvement of the flow predictions. More importantly, DES was able to predict the flow unsteadiness where URANS only predicted a steady flow. The flow predictions were fairly good, with variations between the DES models. The spectra of the lift and drag coefficients were well captured by the DES models. The DES with a halved C_{DES} coefficient appear to be better overall in terms of comparison with experiments. The pressure coefficient on the aerofoil surface was also well predicted.

DES was thereafter applied on the 7A/7AD rotors and compared with both the experiment and URANS models. Both turbulence models predicted quite well the lift and moment coefficients evolution along the rotor rotation. However, DES tended to slightly improve the predictions in the back of the disk and, more importantly, the results contained a broader frequential content. These results are encouraging for further studies, particularly when structural deformations are taken into account, causing higher frequency modes to be excited.

Acknowledgements

The financial support of the Engineering Physical Sciences Research Council (EPSRC) and the U.K. Ministry of Defence (MoD) under the Joint Grant Scheme is gratefully acknowledged for this project. This work forms part of the Rotorcraft Aeromechanics Defence and Aerospace Research Partnership (DARP) funded jointly by EPSRC, MoD, the Department of Trade and Industry (DTI), QinetiQ, and Westland Helicopters.

REFERENCES

[1] J.S. Batten, U.C. Goldberg, and S.R. Chakravarthy. Sub-Grid Turbulence Modeling for Unsteady Flow with Acoustic Resonance. In *38th Aerospace Sciences Meeting, Reno, NV*, 2000. AIAA-00-0473.

[2] L. Dubuc, F. Cantariti, M.A. Woodgate, B. Gribben, K.J. Badcock, and B.E. Richards. A Grid Deformation Technique for Unsteady Flow Computations. *International Journal for Numerical Methods in Fluids*, 32:285–311, 2000.

[3] D. Guenot. *Simulation des effets instationnairesa grande Ãl'chelle dans les Ãl'coulements dÃl'collÃl's*. PhD thesis, SUPAERO, Toulouse, 2004.

[4] A. Jameson. Time Dependent Calculations Using Multigrid, with Applications to Unsteady Flows Past Airfoils and Wings. In *10th Computational Fluid Dynamics Conference, Honolulu, HI*, 1991. AIAA-91-1596.

[5] P. Nayyar, G.N. Barakos, and K.J. Badcock. Numerical study of transonic cavity flows using large-eddy and detached-eddy simulation. *Aeronautical Journal*, 111(1117):153–164, 2007.

[6] S. Osher and S. Chakravarthy. Upwind Schemes and Boundary Conditions with Applications to Euler Equations in General Geometries. *Journal of Computational Physics*, 50(3):447–481, June 1983.

[7] R. Steijl and G. Barakos and K. Badcock. A framework for CFD analysis of helicopter rotors in hover and forward flight. *International Journal for Numerical Methods in Fluids*, 51(8):819–847, 2006.

[8] P.L. Roe. Approximate Riemann Solvers, Parameter Vectors, and Difference Schemes. *Journal of Computational Physics*, 43(2):357–372, October 1981.

[9] T. Rung, U. Bunge, M. Schatz, and F. Thiele. Restatement of the Spalart-Allmaras Eddy-Viscosity Model in Strain-Adaptative Formulation. *AIAA Journal*, 74(7):1396–1399, 2003.

[10] P. Spalart, S. Deck, M.L. Shur, K.D. Squires, M.Kh. Strelets, and A. Travin. A new version of detached-eddy simulation, resistant to ambiguous grid densities. *Theor. Comput. Fluid Dyn.*, 20:181–195, 2006.

[11] P. Spalart, W.H. Jou, M.Kh. Strelets, and S.R. Allmaras. Comments on the feasibility of LES for wings, and on a hybrid RANS/LES approach. In *Advances in DNS/LES, Columbus*, 1997.

[12] P.R. Spalart and S.R. Allmaras. A One-Equation Turbulence Model for Aerodynamic Flows. *La Recherche Aérospatiale*, (1):5–21, 1994.

[13] K.E. Swalwell, J. Sheridan, and W.H. Melbourne. Frequency Analysis of Surface Presssures on an Airfoil After Stall. 21st Applied Aerodynamics Conference, Orlando, Florida, June 23–26 2003. .

Turbulence model	C_L	C_D
Experiment	0.930	1.539
SA	0.579	1.480
SALSA	0.539	1.630
DES	0.739	1.936
DES SALSA	1.106	1.274
DDES	0.718	1.947
DDES SALSA	0.753	2.053
DES halfC_{DES}	0.735	1.879
DES Medium grid	0.780	1.929
DES, NTS grid	0.874	2.056

Table 2: Comparison of the lift and drag coefficient of the NACA0021 aerofoil at an incidence of 60 degrees obtained with various turbulence models and the experiments of Swalwell [13]. These coefficients were obtained through an integration of the pressure at the experimental pressure taps locations.

Case	μ	M_∞	C_T	α_S	θ_0	θ_{1c}	θ_{1s}	β_0	β_{1c}	β_{1s}
Case 1	0.1673	0.1031	0.007	0.0	4.87	-2.2	3.1	2.13	0.11	0.32
Case 2	0.355	0.2180	0.0105	0.0	8.57	1.89	7.56	2.12	0.12	0.51
Case 3	0.390	0.2399	0.005	11.0	14.0	-2.0	4.5	0.0	4.5	0.0

Table 3: ONERA 7A and 7AD flight conditions and trimming for the various simulations. The angles are given in degrees.

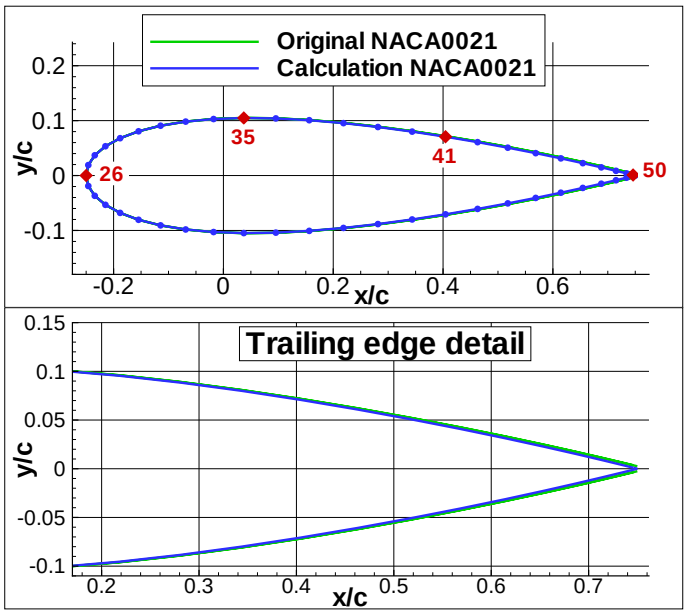

Figure 1: Shape of the NACA0021 aerofoil used for this particular calculation, as well as the tested shape of the NACA0021 aerofoil, with the probe location on a section.

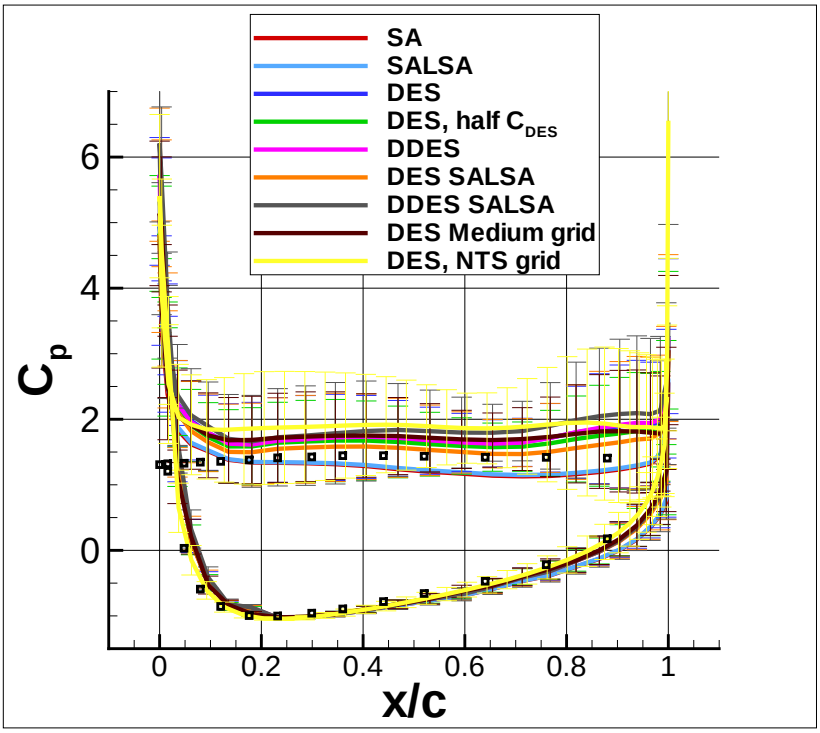

Figure 2: Comparison of the mean pressure coefficient on the NACA0021 aerofoil. The error bars indicate the RMS of the pressure coefficient .

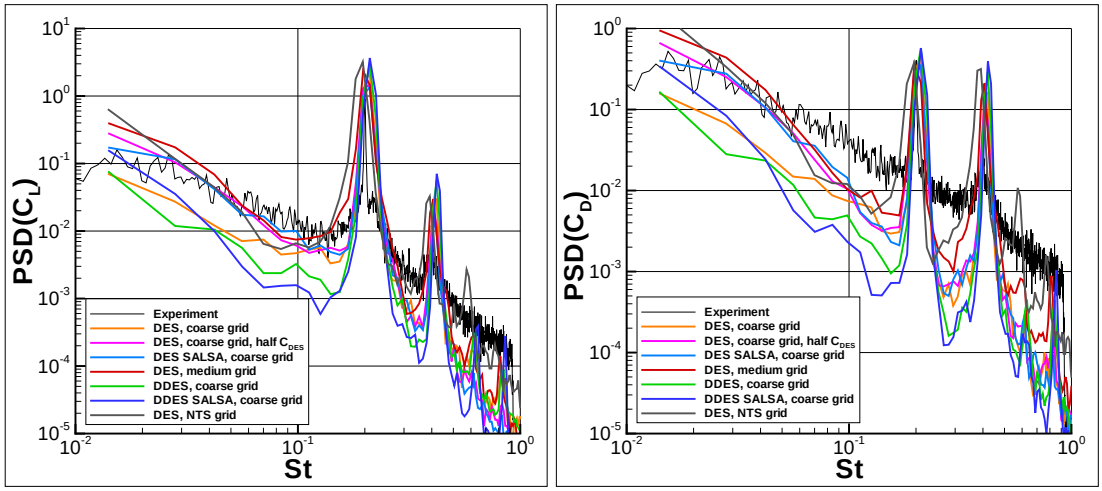

(a) Lift coefficient (b) Drag coefficient

Figure 3: Spectra of lift and drag coefficients obtained with various turbulence models on the coarse and fine grids .

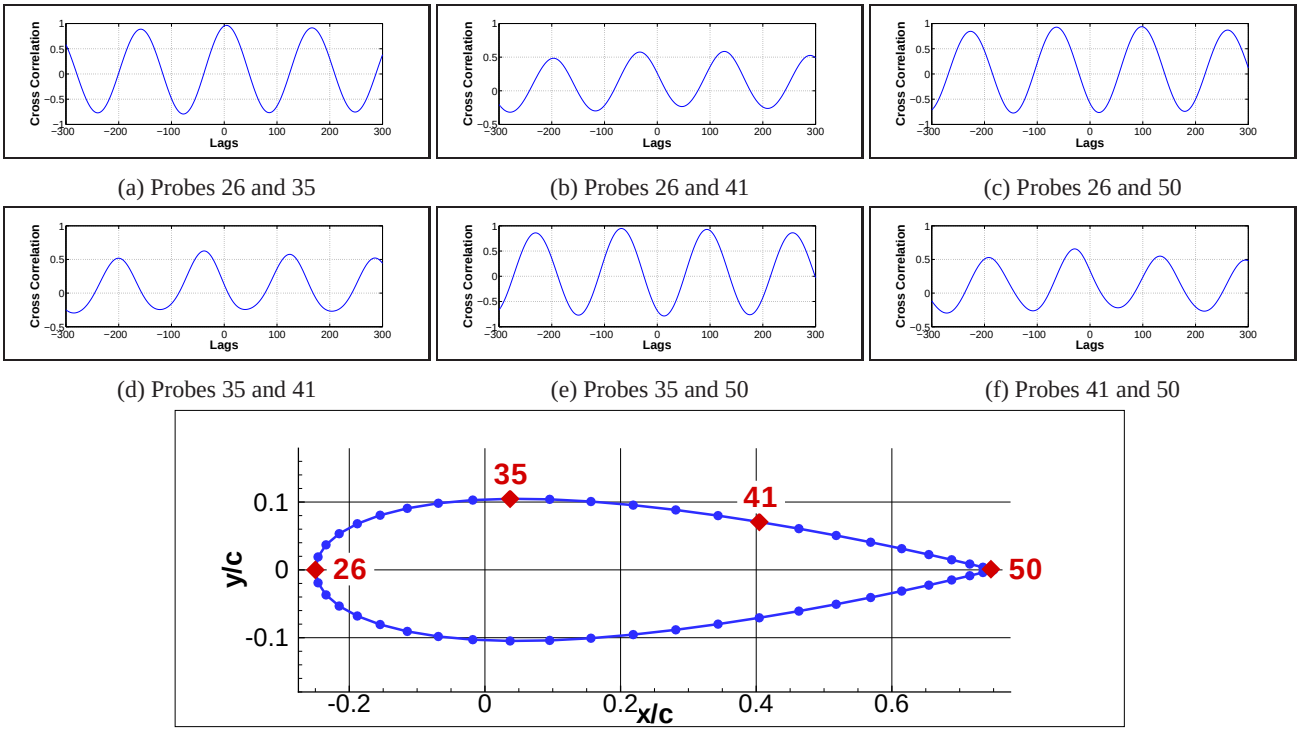

(a) Probes 26 and 35 (b) Probes 26 and 41 (c) Probes 26 and 50

(d) Probes 35 and 41 (e) Probes 35 and 50 (f) Probes 41 and 50

(g) Probe location

Figure 4: Correlation between various probes pressure measurement on the upper surface of the NACA0021 aerofoil at the middle section.

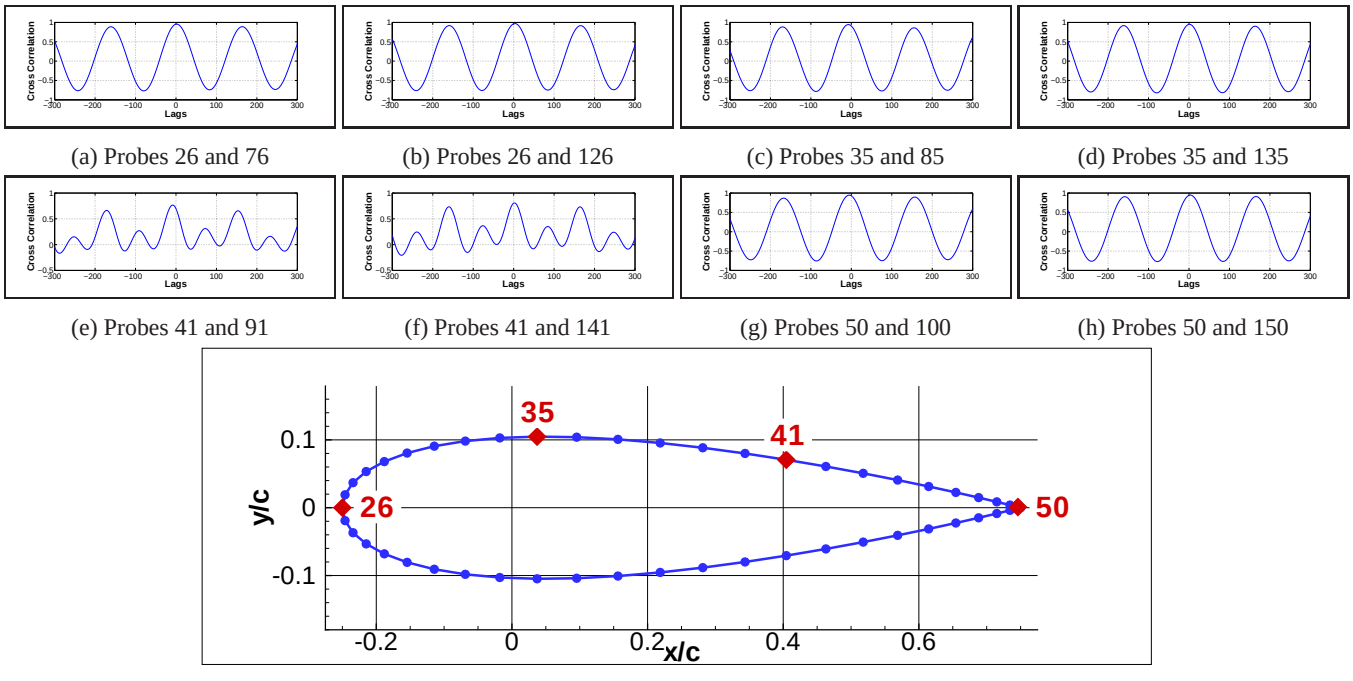

(a) Probes 26 and 76 (b) Probes 26 and 126 (c) Probes 35 and 85 (d) Probes 35 and 135

(e) Probes 41 and 91 (f) Probes 41 and 141 (g) Probes 50 and 100 (h) Probes 50 and 150

(i) Probe location

Figure 5: Correlation of various pressures on the upper surface of the NACA0021 aerofoil between several sections. Probes 76, 85, 91 and 100 in section $z/c = -0.5$ correspond respectively to the locations of probes 26, 35, 41 and 50 on the airfoil section, and the probes 126, 135, 141 and 150 in section $z/c = 0.5$ correspond respectively to the locations of probes 26,35,41 and 50 on the airfoil section

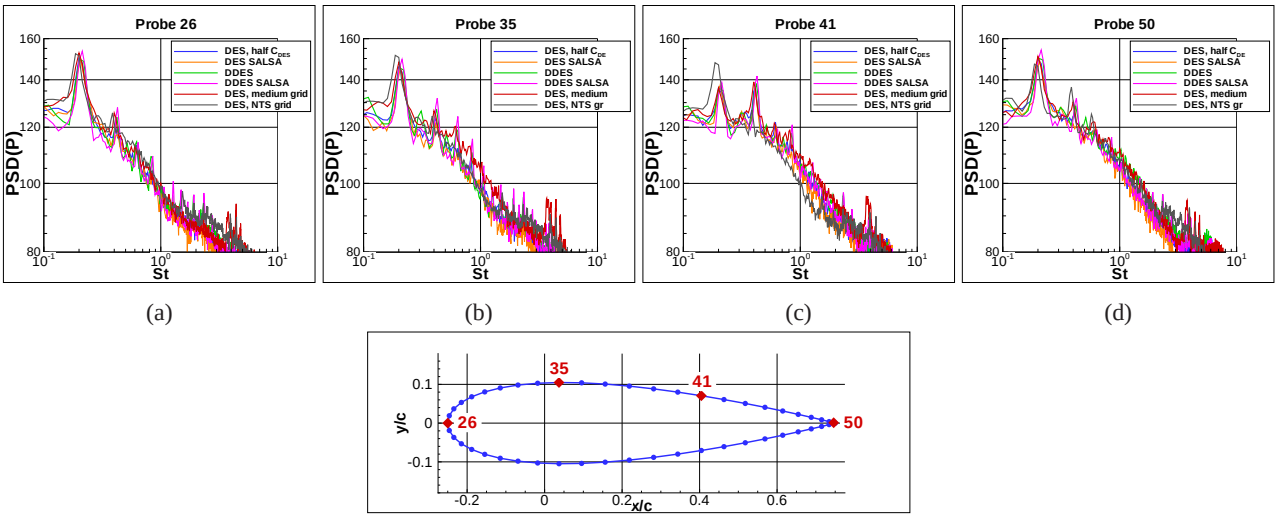

Figure 6: Comparison of the Pressure FFT on the aerofoil surface at various probe locations.

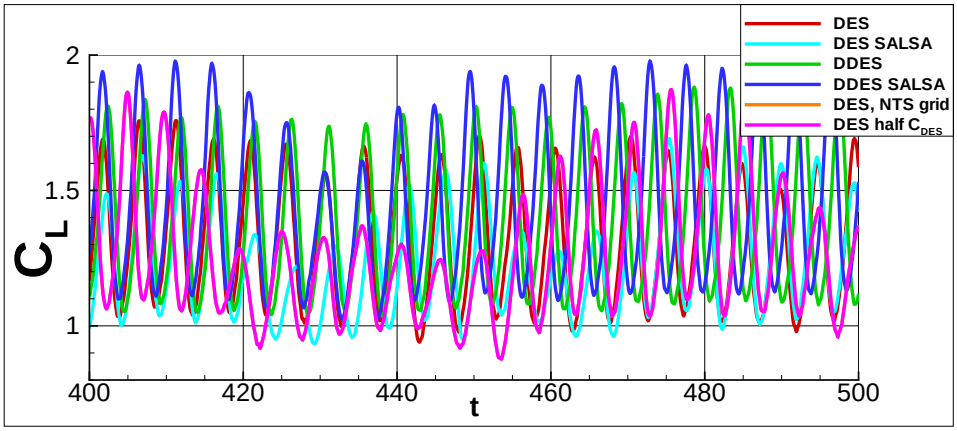

Figure 7: Comparison of lift coefficient evolution during the calculations as a function of dimensionless time, non dimensionalised with c/V_∞. The calculations that converged to a steady state are not shown.

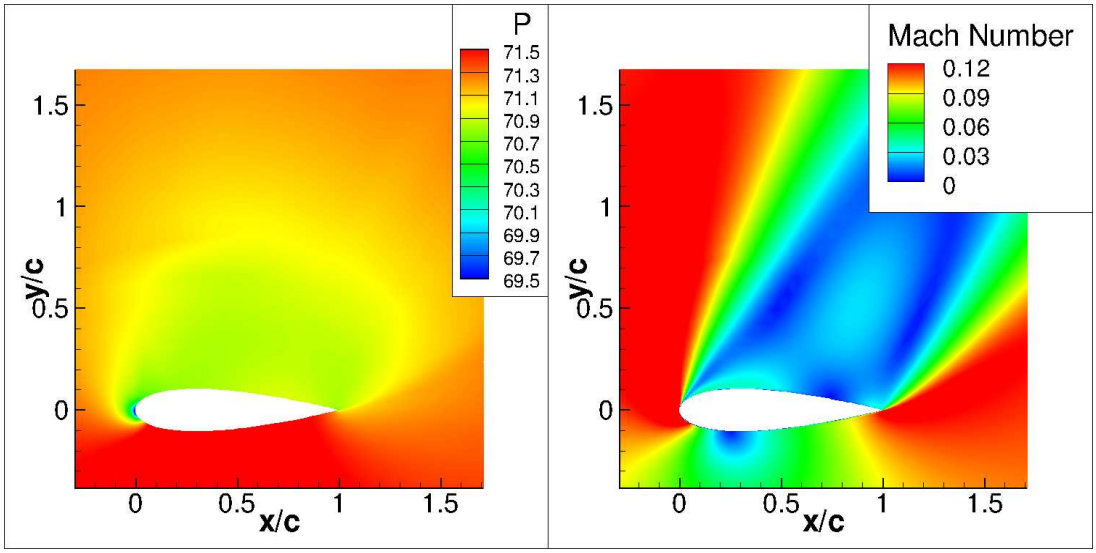

(a) SA

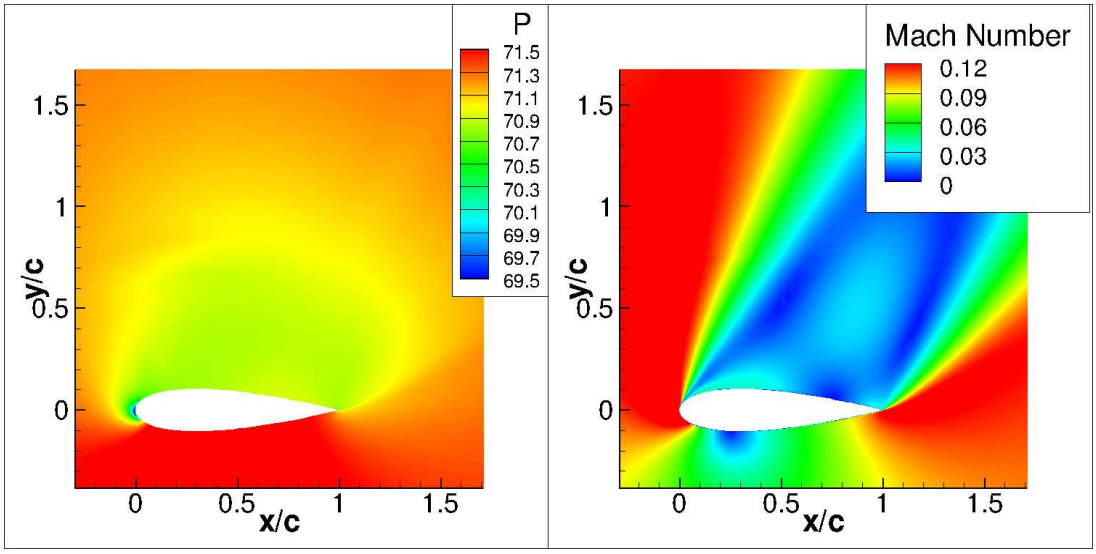

(b) SALSA

Figure 8: Instantaneous dimensionless pressure and Mach number on a slice perpendicular to the wing in its mid-span with both SA and SALSA turbulence models. The pressure is non dimensionalised with $\rho_\infty U_\infty^2$.

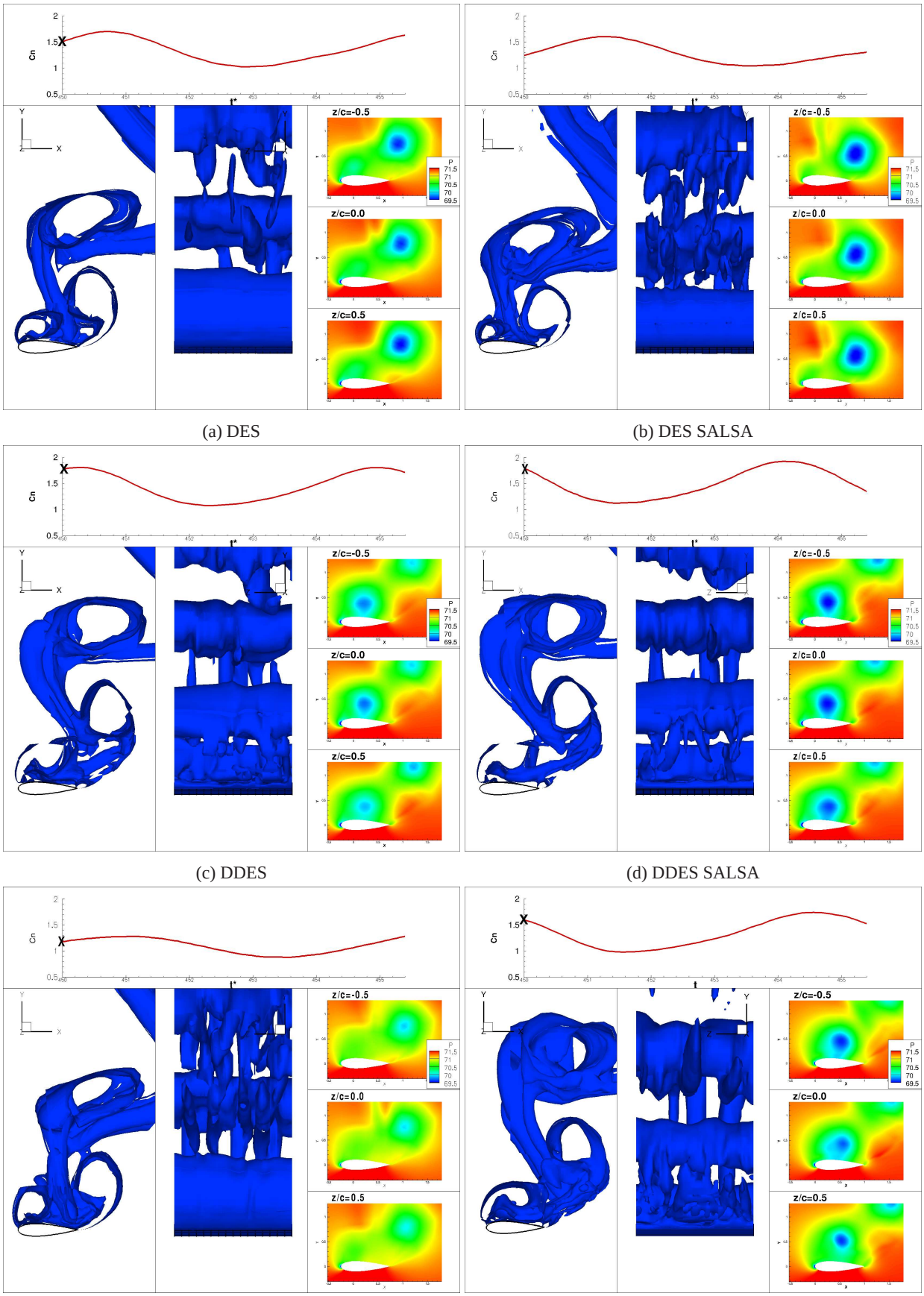

(a) DES

(b) DES SALSA

(c) DDES

(d) DDES SALSA

(e) DES with halved C_{DES}

(f) DES with NTS grid

Figure 9: Comparison of the instantaneous isosurfaces of the Q-criterion at 0.125 and pressure on slices perpendicular to the wing at $z/c = -0.5$, 0 and 0.5 from calculations with various turbulence models at the time step $t = 450c/V_\infty$.

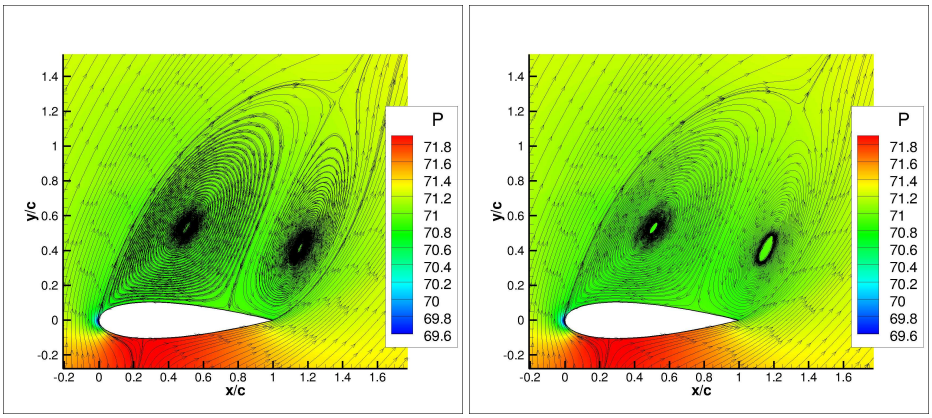

(a) SA (b) SALSA

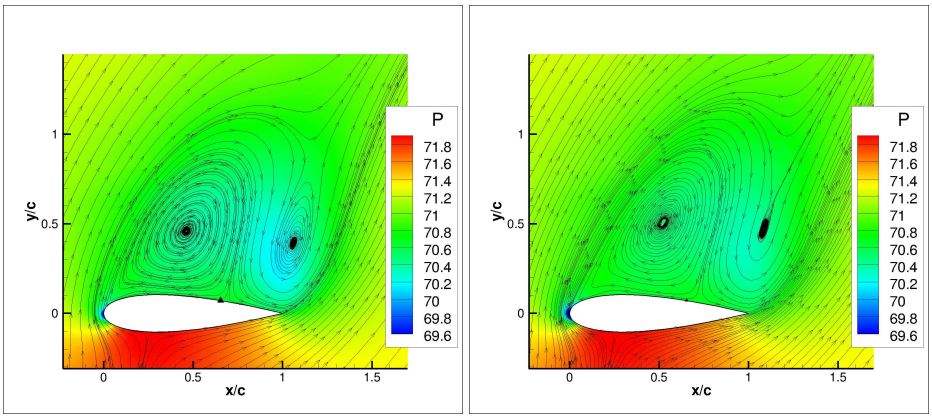

(c) DES (d) DES SALSA

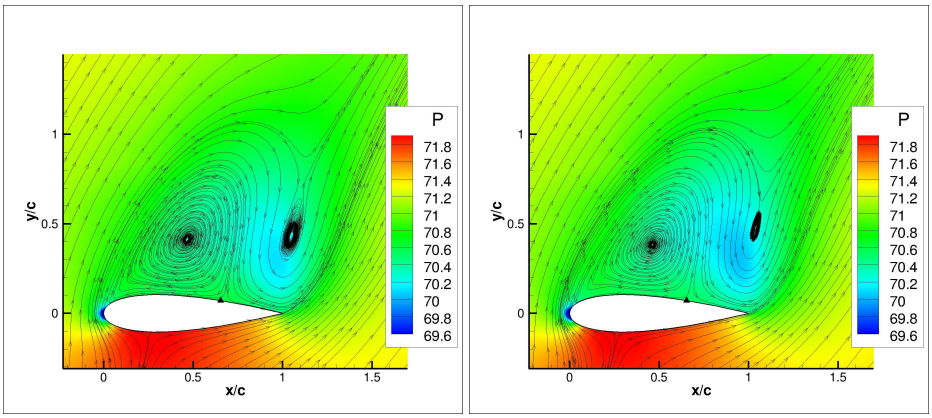

(e) DDES (f) DDES SALSA

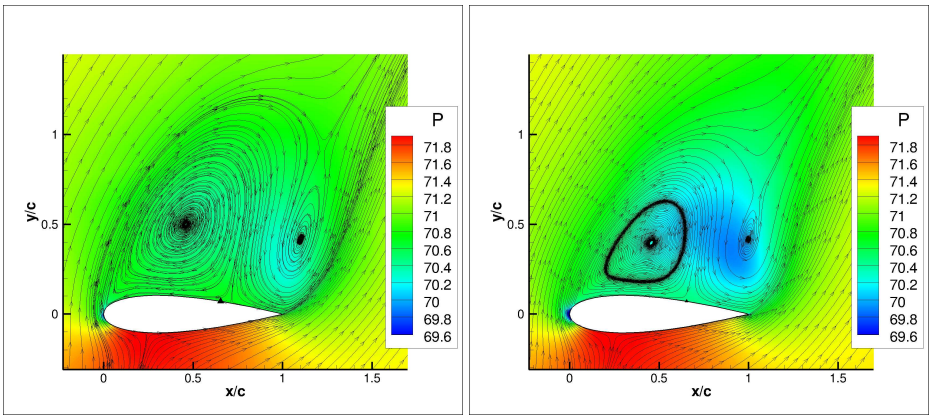

(g) DES half C_{DES} (h) DES, NTS grid

Figure 10: Comparison of the mean pressure and flow on space and time in a plane perpendicular to the wing with URANS and DES turbulence models. The mean flow was obtained through a spatial mean of 9 sections and a temporal mean over a dimensionless time range of 300.

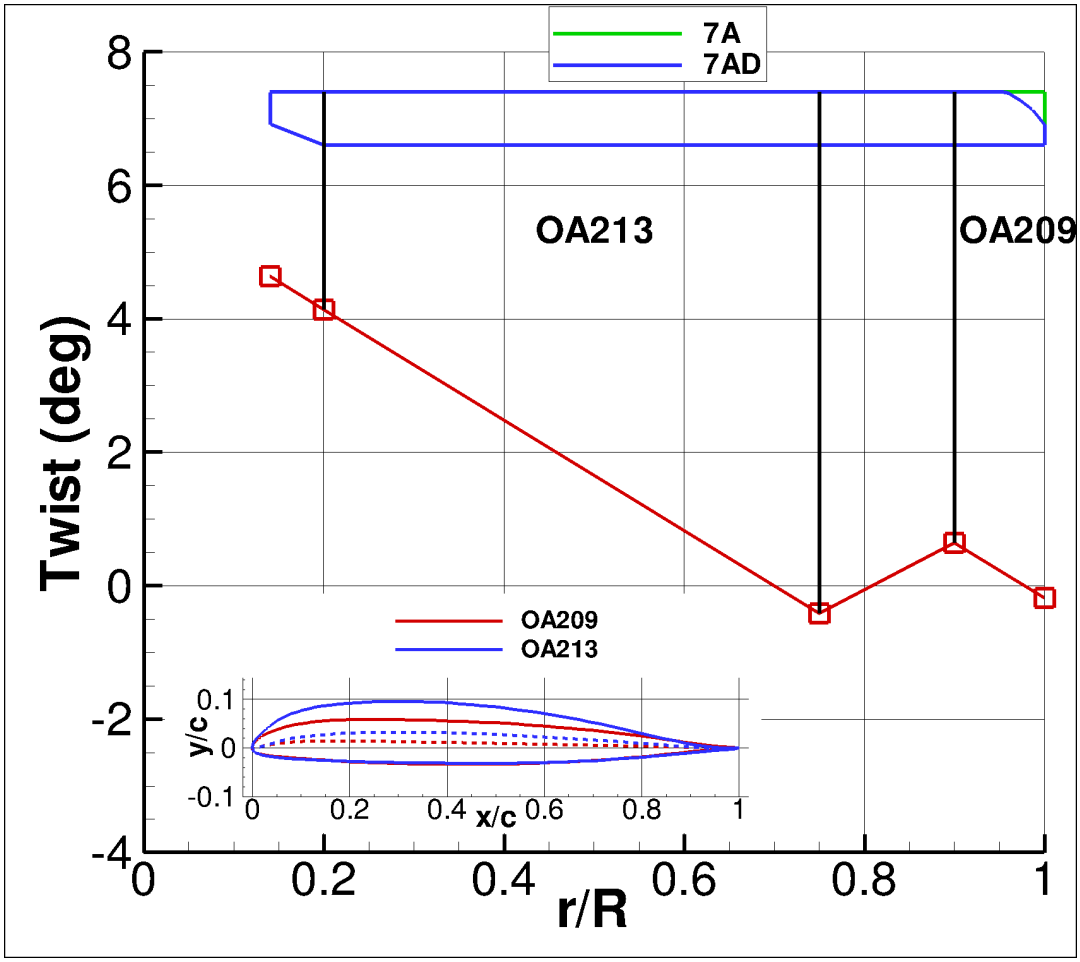

(a) 7A and 7AD rotors properties

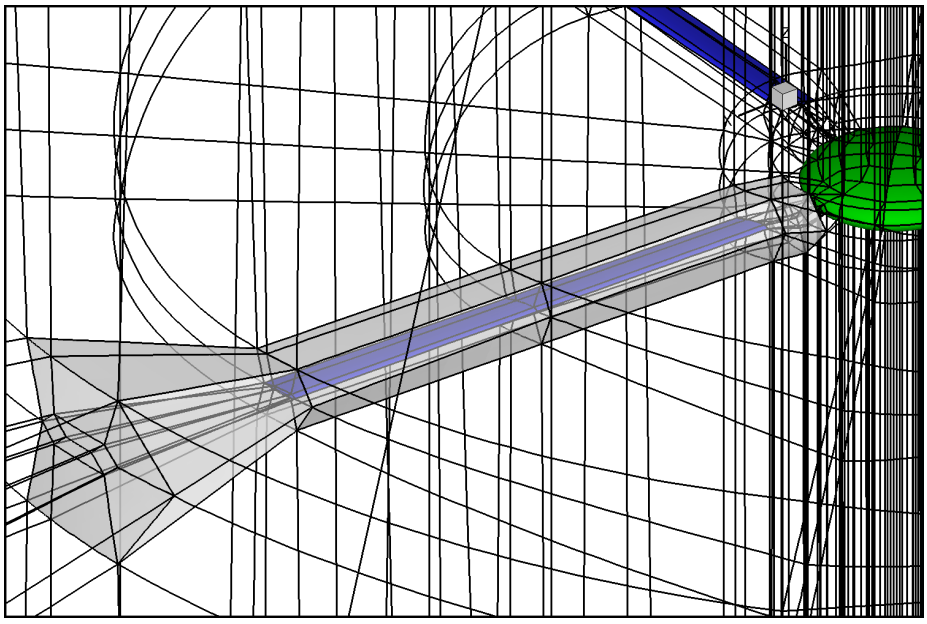

(b) 7A rotor grid topology

Figure 11: Properties of the 7A/7AD rotors and mesh around a forward flying rotor (blades in blue, hub in green and block edges in black).

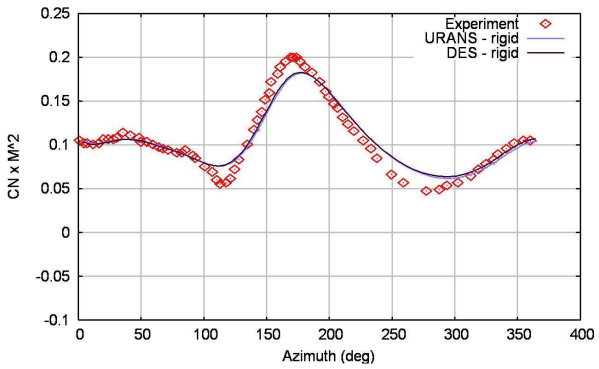

(a) $M^2C_n, r/R = 0.7$

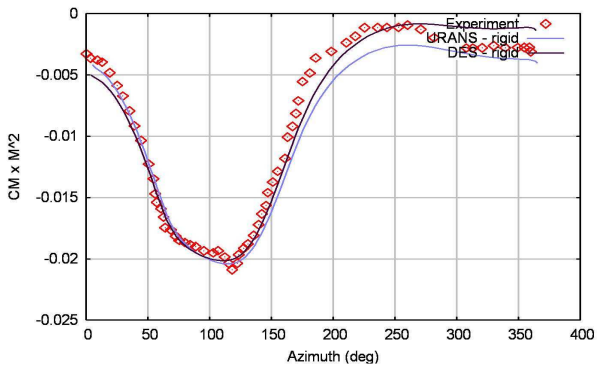

(b) $M^2C_m, r/R = 0.7$

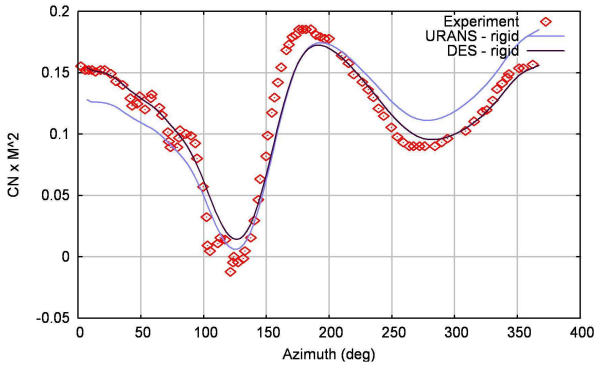

(c) $M^2C_n, r/R = 0.825$

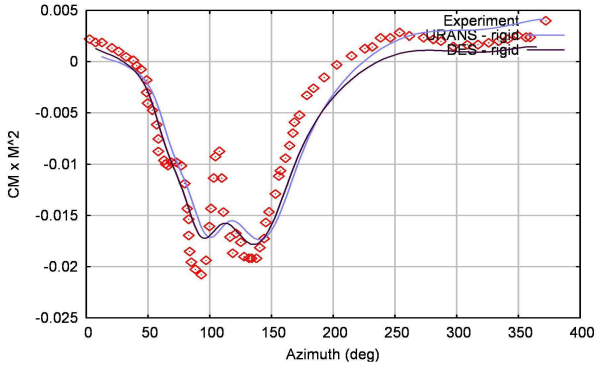

(d) $M^2C_m, r/R = 0.825$

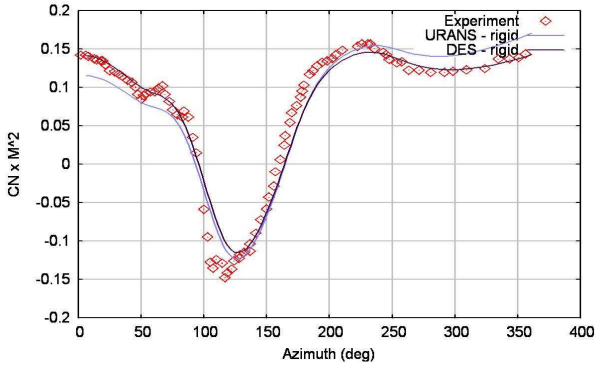

(e) $M^2C_n, r/R = 0.975$

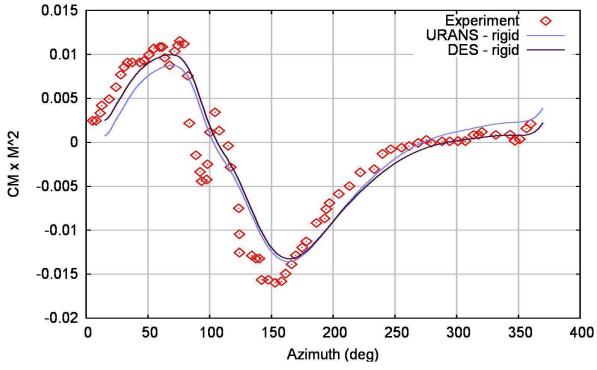

(f) $M^2C_m, r/R = 0.975$

Figure 12: Comparison of the Mach scaled normal and moment coefficients at three sections obtained with URANS and DES turbulence models during a revolution with the experiment for an ONERA 7A rotor in case 3 conditions.

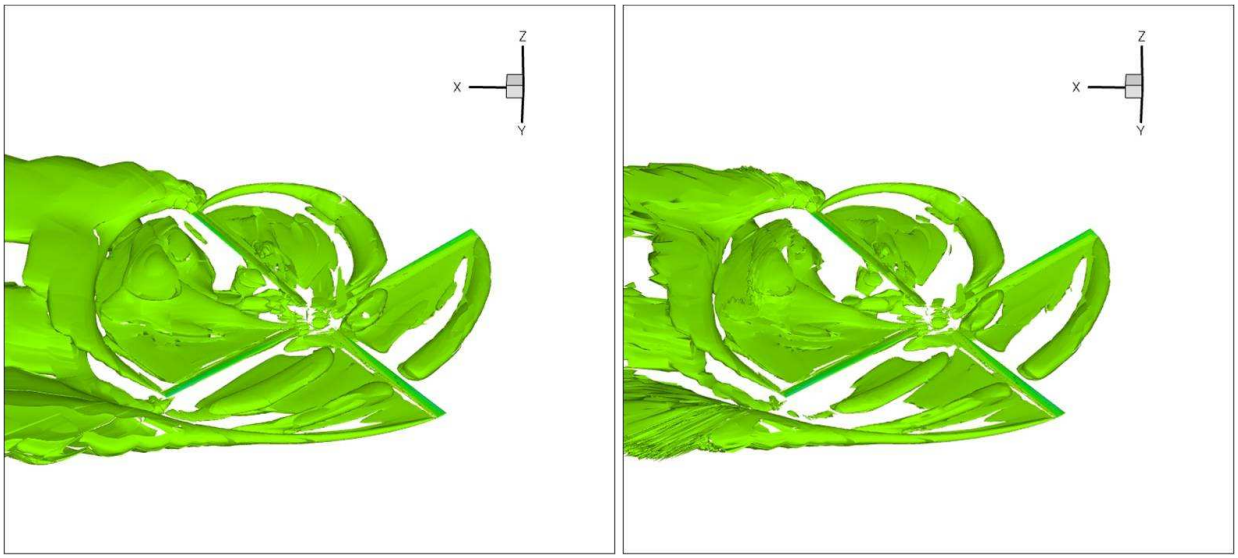

(a) URANS (b) DES

Figure 13: λ_2 isosurfaces comparison for URANS and DES turbulence models simulations.

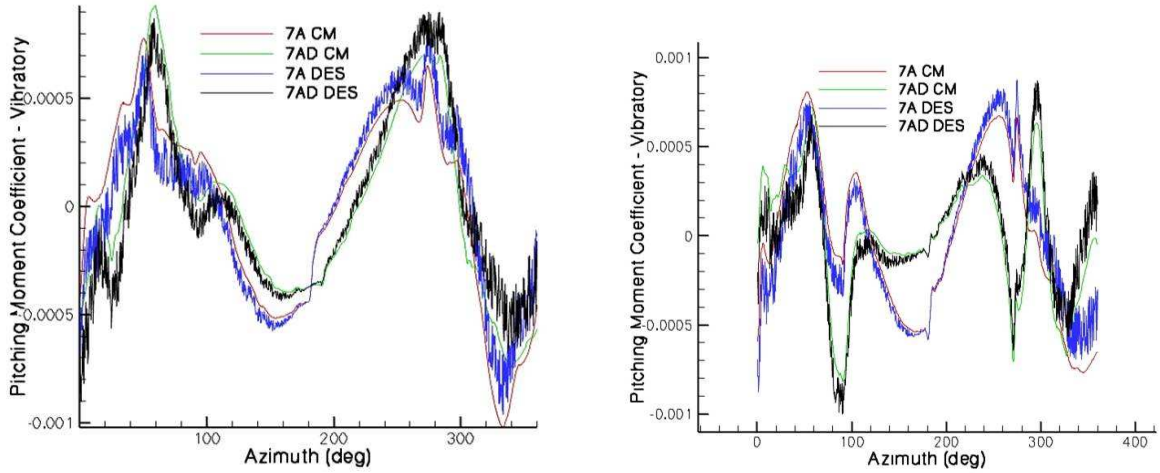

(a) Case 1 (b) Case 2

Figure 14: Comparison of the pitching moments vibratory part for the 7A and 7AD rotors during a revolution for two test cases.